Electron Paramagnetic Resonance Implemented with Multiple Harmonic Detections Successfully Maps Extracellular pH In Vivo

Ririko Nakaoka, Kazuhiro Kato, Kumiko Yamamoto, Hironobu Yasui, Shingo Matsumoto, Igor A. Kirilyuk, Valery V. Khramtsov, Osamu Inanami, and Hiroshi Hirata*

Cite This: *Anal. Chem.* 2023, 95, 3940−3950

Read Online

ACCESS | 📊 Metrics & More | 📖 Article Recommendations | 🆂🅸 Supporting Information

ABSTRACT: Extracellular acidification indicates a metabolic shift in cancer cells and is, along with tissue hypoxia, a hallmark of tumor malignancy. Thus, non-invasive mapping of extracellular pH (pHe) is essential for researchers to understand the tumor microenvironment and to monitor tumor response to metabolism-targeting drugs. While electron paramagnetic resonance (EPR) has been successfully used to map pHe in mouse xenograft models, this method is not sensitive enough to map pHe with a moderate amount of exogenous pH-sensitive probes. Here, we show that a modified EPR system achieves twofold higher sensitivity by using the multiple harmonic detection (MHD) method and improves the robustness of pHe mapping in mouse xenograft models. Our results demonstrate that treatment of a mouse xenograft model of human-derived pancreatic ductal adenocarcinoma cells with the carbonic anhydrase IX (CAIX) inhibitor U-104 delays tumor growth with a concurrent tendency toward further extracellular acidification. We anticipate that EPR-based pHe mapping can be expanded to monitor the response of other metabolism-targeting drugs. Furthermore, pHe monitoring can also be used for the development of improved metabolism-targeting cancer treatments.
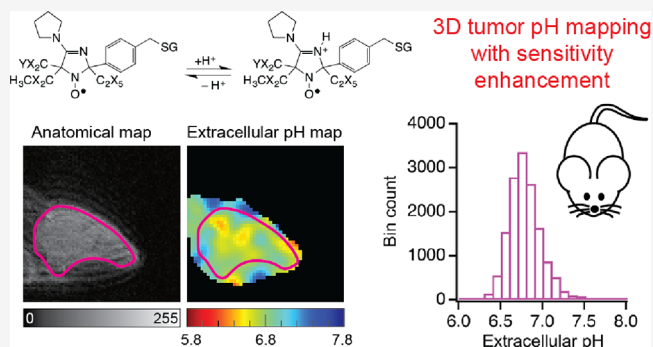
Extracellular acidification in solid tumors is a hallmark of tumor malignancy, along with tissue hypoxia.[1] This extracellular acidification reflects a shift in tumor metabolism, such as upregulated glycolysis in malignant tumors. Typically, the tumor microenvironment (TME) of solid tumors can be characterized by extracellular acidification, or acidosis,[2] which has been shown to facilitate the migration, invasion, and metastasis of cancer cells[3] and is thus an indicator of malignancy.[4] Therefore, non-invasive mapping of extracellular acidification is essential for researchers to understand the TME and to monitor the response of solid tumors to metabolism-targeting drugs.

Regulation of the pH of cancer cells is essential for the survival of malignant tumors with metabolic shifts.[5] The expression of proteins involved in the glycolytic system, such as glucose transporter 1 (GLUT1) and monocarboxylate transporter 4 (MCT4), is increased in cancer cells compared to normal cells, and glucose metabolism is accelerated, which is thought to cause acidification around cancer cells due to the release of glucose-derived lactate by MCT4.[6,7] Upregulated glycolysis of cancer cells results in overproduction of lactic acid and protons.[8] However, some transporters and enzymes, such as carbonic anhydrase IX (CAIX), are involved in cellular pH homeostasis.[9] CAIX converts carbon dioxide to bicarbonate and a proton. An anion exchange transporter then shuttles bicarbonate into the cell, where the bicarbonate is converted back to carbon dioxide in a process that consumes a proton. Due to upregulated glycolysis and the activities of transporters and enzymes mentioned above, the extracellular medium is acidified and intracellular pH is controlled to be slightly alkaline. Moreover, CAIX acts as extracellular pH (pHe)-stat and thus sets a specific level of acidification in the TME.[10]

Numerous in vivo pHe monitoring and mapping techniques for malignant tumors have been reported. For example, fluorescence imaging[11,12] is capable of mapping pHe with a high spatial resolution. However, high optical absorption and scattering in biological tissues are significant obstacles for non-invasive detection of pH deep in tissue. Nuclear magnetic resonance (NMR) techniques can overcome these limitations, but a long imaging time and limited sensitivity for exogenous pH-sensitive probes are drawbacks.[13−17] Hyperpolarized ^{13}C-magnetic resonance imaging (MRI) solved the sensitivity issue of a ^{13}C-labeled imaging agent; however, the image acquisition time is limited.[13,14] Recently, multislice acquisition in chemical
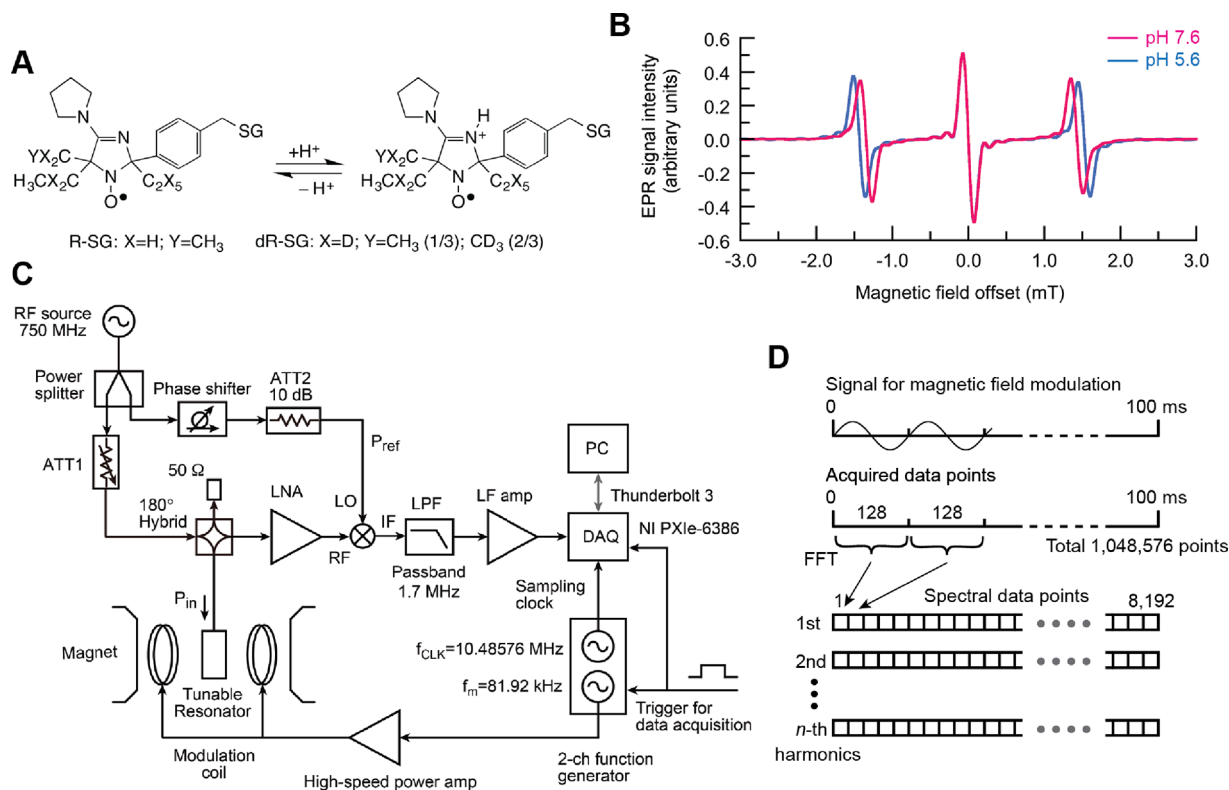
Figure 1. EPR-based pH measurement setup. (A) Unprotonated and protonated forms of the pH-sensitive free radical probe dR-SG exhibit different hyperfine splitting constants. SG stands for glutathione residue. (B) The first-derivative EPR absorption spectra for dR-SG at 5.6 and 7.6 pH and 37 °C. (C) EPR spectrometer setup with the MHD receiver system (for simplicity, magnetic field gradient coils and power supplies for the magnetic field gradients are not shown). (D) The signal acquisition and spectral data processing scheme. To record 8192 spectral data points for the nth harmonics, the voltage signal of the low-frequency (LF) amplifier output was digitized over a period of 100 ms. The details of the radiofrequency (RF) and electronic components used in the EPR spectrometer are listed in Supplementary Table 1.

exchange saturation transfer (CEST) MRI has been developed, making multislice pH mapping possible.[18,19] However, the limited sensitivity issue for exogenous probes is still present for CEST-MRI and requires a higher probe concentration for animal experiments.

Electron paramagnetic resonance (EPR) has a higher sensitivity than nuclear MR for the same numbers of nuclear and electron spins because the electron gyromagnetic ratio is 658 times higher than the gyromagnetic ratio of proton.[20] EPR-based pHe mapping was previously applied to mouse xenograft models with a pH-sensitive free radical probe.[21] We mapped progress in extracellular acidification during tumor growth of a murine tumor model and different pHe distributions for mouse xenograft models of three human-derived pancreatic ductal adenocarcinoma cell lines. However, this method is not sensitive enough to map pHe with the moderate amount of exogenous pH-sensitive probes because the spectral absorption linewidth of the pH-sensitive nitroxyl radical dR-SG (Figure 1A) is relatively broad (peak-to-peak intrinsic linewidth 0.13 mT) compared to triarylmethyl radical OX063, which is commonly used in EPR oxygen mapping. Such a broad absorption lineshape leads to a lower signal intensity. The sensitivity of EPR detection is always crucial for in vivo small-animal experiments because the reduction reaction and excretion of free radical probes in a subject mouse decrease the EPR signal from the exogenously injected free radical probes.[22] Therefore, increasing the detection sensitivity of the EPR spectrometer should facilitate pHe mapping in vivo and reduce the amount of free radical probes

exogenously injected. The pH-sensitive nitroxyl radical dR-SG (Figure 1A) is suitable for tumor pHe mapping in vivo for the following reasons. First, the spectral lineshape change is highly sensitive at a slightly acidic pH because the pKa of dR-SG is 6.60 at 37 °C (Figure 1B). Second, dR-SG is confined to the extracellular medium because it does not penetrate the cell membrane.

Multiple harmonic detections (MHDs) enhance the EPR sensitivity and recover the lineshape even with overmodulation in a continuous-wave (CW) detection scheme using magnetic field modulation.[23–26] An MHD approach in EPR spectroscopy has recently been applied to small-animal experiments[26] and is rapidly gaining popularity in EPR imaging. However, no pH mapping with MHD in EPR has yet been demonstrated. We seek an MHD receiver system having no additional distortion of the lineshape to show the feasibility of EPR-based pH mapping using MHD. This is because the distortion of the spectral lineshape in four-dimensional (4D) spectral–spatial EPR imaging degrades the accuracy and resolution of three-dimensional (3D) pH mapping. Therefore, it is crucial for EPR-based pH mapping to demonstrate that MHD in EPR applies to in vivo 3D pH mapping for mouse tumor models without any drawbacks. The application of EPR with MHD to 3D spectroscopic mapping is not trivial because all control and acquisition techniques for 4D spectral–spatial imaging work properly as well as the 4D image reconstruction. Specifically, overmodulation of EPR absorption in MHD requires a large amplitude of magnetic field modulation in pH mapping since pH-sensitive nitroxyl radicals have absorption linewidths one

order of magnitude broader than those of triarylmethyl radicals. A large amplitude of magnetic field modulation beyond a usual modulation level may degrade the baseline stability of CW-EPR detection due to the electromagnetic force induced by eddy currents in a radiofrequency resonator, leading to the inaccuracy of 4D image reconstruction and, ultimately, errors in the resultant pH maps. To enhance sensitivity even with modest overmodulation, the MHD settings, i.e., the number of signal acquisitions, the time window for fast Fourier transform (FFT), and a filtering profile in MHD spectral reconstruction, should be optimized. Moreover, systematic pH measurement errors must be suppressed to achieve excellent accuracy in 3D pH mapping. These optimizations allow sensitivity enhancement without excessive overmodulation for EPR absorption, which is an insight into the MHD approach. If the results verified the ability of our system to detect a shift in tumor pHe, it would indicate that in vivo pHe mapping can be a valuable tool for assessing the therapeutic outcome of CAIX inhibition early.

Furthermore, enhancement of the sensitivity of EPR is essential for extending the applicability of EPR-based pH mapping to various mouse tumor models. However, the impacts of such enhancement of the sensitivity of EPR using MHD on in vivo 3D pH mapping of mouse tumor models remain unclear. Therefore, studies on the applicability of EPR using MHD to in vivo pH mapping are essential for proving that EPR implemented with MHD successfully maps extracellular pH in vivo.

Here, we aimed to develop a modified EPR system that can accurately map the pHe shifts in tumors in vivo. Specifically, we used CW-EPR imaging at 750 MHz coupled to a purposely built MHD receiver system to enhance the performance of the imaging system, which resulted in a twofold sensitivity enhancement over standard EPR imaging. We then used this setup to map the pHe of mouse xenograft models of the human-derived pancreatic ductal adenocarcinoma cell line MIA PaCa-2 and found some benefits from the sensitivity enhancement. Moreover, we were able to monitor the tumor pHe response to the CAIX inhibitor U-104 with this system and the delay in tumor growth. Finally, we showed the feasibility of in vivo pHe mapping using EPR for pharmacological intervention in tumor xenograft models. This pHe mapping can be expanded to monitor the pHe response to other metabolism-targeting drugs.

■ EXPERIMENTAL SECTION

EPR Spectrometer and Imager. Figure 1C shows a simplified diagram of the laboratory-built 750 MHz CW-EPR spectrometer used in this study. The configurations of the EPR spectrometer and imager were previously reported.[27,28] This spectrometer can acquire EPR spectra faster than a commercially available CW-EPR spectrometer by one order of magnitude.[27,28] This advantage is essential to obtaining thousands of EPR spectra from a mouse xenograft model in 3D pHe mapping in vivo. Conventionally, we used a lock-in amplifier for phase-sensitive detection (PSD) in conjunction with magnetic field modulation. For MHD, a 16-bit digital acquisition (DAQ) board (PXIe-6386, National Instruments, Austin, Texas), with a maximum sampling rate of 14 MS s^{-1} per channel, was used to receive the voltage signal of an LF amplifier after RF homodyne detection. The digitized data were transferred to a computer through a Thunderbolt 3 interface for signal processing. The frequency of magnetic field

modulation was set to 81.92 kHz, determined by the data sampling duration (100 ms) and the number of spectral data points (8192) per scan (Figure 1D). Each spectral data point corresponded to a cycle of magnetic field modulation. These data points in signal acquisition and processing influence the signal-to-noise ratio (SNR) of the reconstructed EPR spectrum. We empirically optimized the number of data points to enhance the sensitivity of EPR. A sampling frequency of 10.48576 MHz, 128 times higher than the frequency of the magnetic field modulation, was set to synchronize the signal sampling to the magnetic field modulation. These two signals were generated and synchronized with a dual-channel function generator (33522A, Keysight Technologies, Santa Rosa, California), and further synchronization was achieved with an external trigger controlled by magnetic field scanning and field gradients. A multicoil parallel-gap resonator (22 mm in diameter and 30 mm long for the sample space) was used in the spectrometer.[27,29] The conversion efficiency of the RF magnetic field was 126 μT/W$^{1/2}$ at the center of the unloaded resonator. Our resonator (22 mm in diameter) is large enough to accommodate a tumor-bearing leg; however, a larger resonator, such as one 35 mm in diameter, would be helpful for measuring a variety of tumor models since such a resonator can accommodate the abdomen of a subject mouse. The saddle coil for magnetic field modulation was fixed to a hollow bobbin. For PSD, a digital lock-in amplifier (LI5640, NF Corp., Yokohama, Japan) was used for EPR signal detection.

Chemicals. The pH-sensitive nitroxyl radical dR-SG, a deuterium-enriched analogue of R-SG (2-(4-((2-(4-amino-4-carboxybutanamido)-3-(carboxymethylamino)-3-oxopropylthio)methyl)phenyl)-4-pyrrolidino-2,5,5-triethyl-2,5-dihydro-1H-imidazol-1-oxyl), and R-SG itself was synthesized as previously reported.[30] The CAIX inhibitor U-104 was purchased from MedChemExpress (product no. HY-13513, Monmouth Junction, New Jersey, USA).

Signal Processing with the MHD Receiver System. The MHD receiver system was built using the LabVIEW 2020 development environment (National Instruments, Austin, Texas). The above data acquisition and signal processing were coded using the producer/consumer design pattern in LabVIEW; this code can be used to separate data acquisition and signal processing and run them in parallel to obtain multiple harmonics and EPR spectra (the LabVIEW code is presented at https://github.com/hu-mre/mhd-acquisition-and-processing). Data acquisition and signal processing were performed on a personal computer (Intel Core i7, 3.2 GHz, memory 16 GB).

Computation of the first-derivative spectrum from the multiple harmonic signals, called spectral lineshape reconstruction, was conducted in the Fourier domain based on a previously reported method.[24,25] The mathematical expression of the spectral lineshape reconstruction is given in the Supporting Information. The Fourier transform of the first-derivative EPR absorption spectrum of the sample is filtered by a square window convoluted with the Gaussian function. The cutoff point of this low-pass filter should be optimized for recovering the spectral linewidth due to the tradeoff between the SNR and the linewidth of the reconstructed spectrum. Excessive low-pass filtering for spectral lineshape reconstruction affects the resultant lineshape, leading to pH measurement errors. Therefore, these errors must be considered for this filtering setting. The obtained first-derivative spectrum was further processed to determine the pH value using the
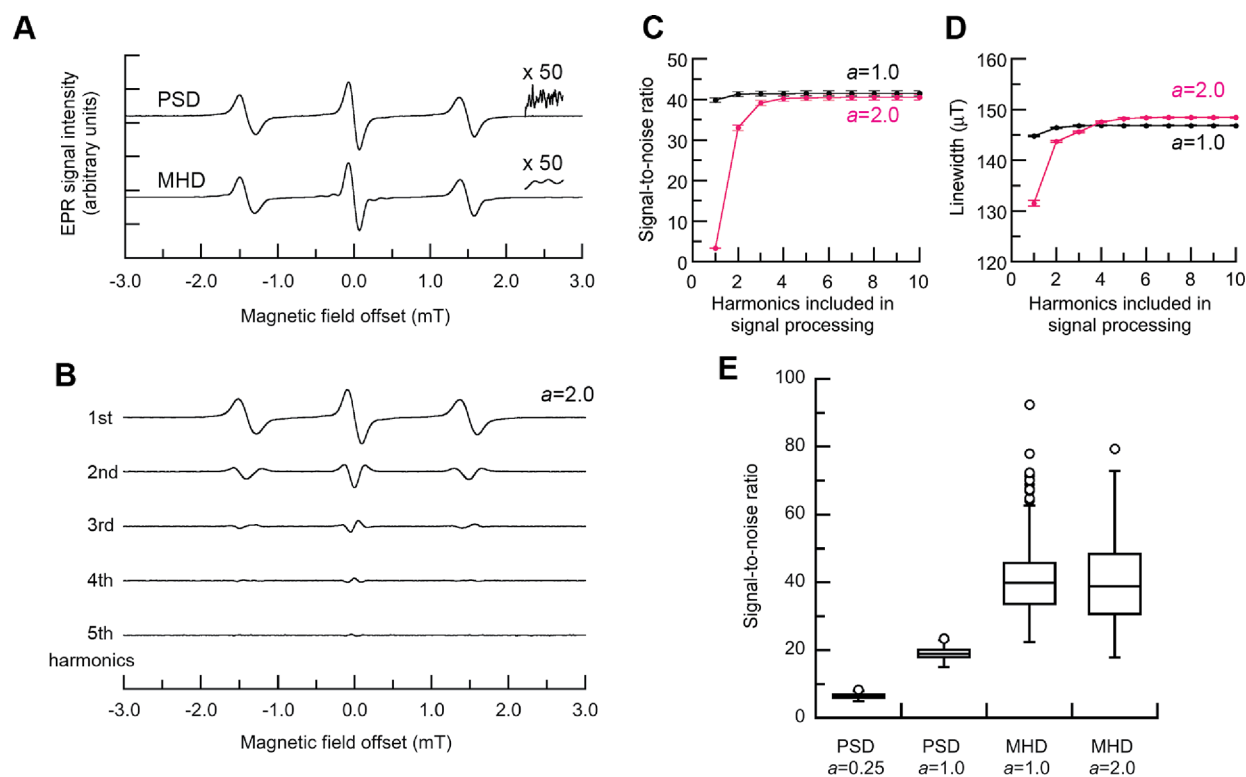
Figure 2. Multiple harmonic detections and spectral reconstruction. (A) First-derivative EPR absorption spectra recorded with phase-sensitive detection (PSD) and multiple harmonic detection (MHD) schemes (modulation ratio $a = 1.0$). (B) First to fifth harmonic spectra of dR-SG (modulation ratio $a = 2.0$). (C) Signal-to-noise ratio as a function of the number of harmonics involved in MHD ($a = 1.0$ and 2.0). (D) Peak-to-peak linewidth of the central spectral peak ($a = 1.0$ and 2.0). (E) Comparison of the signal-to-noise ratios between EPR spectra obtained with PSD and MHD (sample size $n = 300$). In (C) and (D), plots and error bars represent the mean ± standard error (SE). Circles in (E) are outliers. The pH-sensitive probe dR-SG was dissolved in 2 mL of phosphate-buffered saline, and its concentration was 2 mmol L^{-1}.

mathematical model[21] of the spectral lineshape for a known-pH solution.

Solution Samples. dR-SG (2 mmol L^{-1}) was dissolved in phosphate-buffered saline. Seven radical solutions with pH values ranging from 6.20 to 7.40 were prepared by adding HCl or NaOH to the dissolved dR-SG. The solution pH was measured with a pH meter (SevenCompact pH meter S220, Mettler Toledo, Columbus, Ohio) equipped with a glass electrode (InLab Semi-Micro, Mettler Toledo, Columbus, Ohio). The solutions were placed in individual 2 mL vials of inner diameter 9.8 mm and length 32 mm (product no. 5182-0715, Agilent Technologies, Santa Clara, California). The solutions were then air saturated and stored in a refrigerator at 4 °C until the pH mapping.

pH Mapping of Solution Samples. The following measurement settings were used for EPR image acquisition with both conventional PSD and digital MHD systems: magnetic field scan duration 100 ms, magnetic field scanning 9.0 mT, magnetic field modulation 0.13 mT, modulation frequency 81.92 kHz, maximum field gradient 70 mT m^{-1}, and incident RF power 2.2 mW. The lock-in amplifier time constant was set to 30 μs for the conventional PSD system, and the number of data points was 2048 per scan. For the digital MHD system, the cutoff frequency of the low-pass filter (LPF) for the nth harmonic spectrum in the Fourier domain was 2604 Hz, corresponding to a time constant of 30 μs in the lock-in amplifier. The cutoff data point was set to the 50th data index in the Fourier domain, the number of spectral data points was 8192, and the number of harmonics involved in the MHD reconstruction was 4. The spectral projections were acquired at

$15 \times 15 \times 15$ field gradients for the X-, Y-, and Z-directions (a total of 3375 projections). The total acquisition time was 7.5 min. pH mapping of the radical solutions was performed at 37 °C at a spatial resolution approximately estimated as the ratio of the peak-to-peak line width for dR-SG (0.147 mT at 2 mmol L^{-1} concentration; see Figure 2) to the maximum field gradient (70 mT m^{-1}), or 2.1 mm.

The pH value was computed from the ratio of the signal intensities corresponding to the unprotonated and protonated forms of dR-SG. The details of pH computation have been previously reported.[21] Briefly, we used the following equation to estimate the pH value (pH_{EPR}) from the reconstructed EPR spectrum at each voxel:

$$pH_{EPR} = pKa + \log_{10} \frac{\sum a_i[R]_i}{\sum a_i[RH^+]_i} \tag{1}$$

where $[RH^+]_i$ and $[R]_i$ are the known concentrations of protonated and unprotonated forms of the radical for the ith prepared known sample. Coefficient a_i is the weighting factor for a linear combination of multiple spectra of known pH solutions to best fit the reconstructed spectrum. Since we used the ratio of the two forms of the dR-SG radical, as shown in eq 1, the dR-SG radical loses sensitivity to the pH in the solution when the pH value is far from pKa.

To reduce pH measurement errors, the EPR-based pH value (pH_{EPR} obtained by eq 1) can be corrected using the fitted curve of the measured pH values. We computed the corrected pH value ($pH_{corrected}$) as follows:

$$\text{pH}_{\text{corrected}} = \text{pH}_{\text{EPR}} + (0.0116 + 0.2257x + 0.2592x^2 + 6.945\text{x}10^{-3}x^3) \quad (2)$$

where $x = \text{pH}_{\text{EPR}} - \text{pKa}$. This correction of the measured values improves the linearity of the EPR-based pH measurements.

pH Image Reconstruction. To obtain 3D pH maps, 4D spectral−spatial EPR images were reconstructed by an iterative algebraic reconstruction technique (ART), with spectral data fitting at each iteration.[21] ART computation was performed on an Apple Mac mini (M1, memory 8 GB). The reconstruction code for pH mapping was previously reported.[21,31] The 4D EPR images of the solution samples were reconstructed with a matrix size of $768 \times 48 \times 48 \times 72$, corresponding to a spectral window of 6.75 mT and a field of view (FOV) of 25.0 mm × 25.0 mm × 37.5 mm. In image reconstruction, the isotropic voxel size was 0.52 mm; however, the spatial resolution of pH mapping was 2.1 mm in all three orthogonal directions, as mentioned in the previous subsection. For pH mapping of the tumor-bearing mouse legs, the image matrix was $768 \times 48 \times 48 \times 48$ and the spectral window and FOV were set to 6.75 mT and 25.0 mm × 25.0 mm × 25.0 mm, respectively. The computations in ART were terminated at the seventh iteration for MHD and the ninth iteration for PSD, sufficient for minimizing the overall error in the pH measurements:

$$\text{error} = \frac{1}{m}\sum_{i=1}^{m} |\text{pH}_{\text{median}}(i) - \text{pH}_{\text{electrode}}(i)| \quad (3)$$

where m is the number of prepared samples, $\text{pH}_{\text{median}}$ is the median of the reconstructed pH values, and $\text{pH}_{\text{electrode}}$ is the pH value measured with the electrode pH meter. Surface-rendered images and two-dimensional (2D) images were depicted using IDL 8.7 (L3Harris Geospatial, Bloomfield, Colorado, USA) and ImageJ (http://rsb.info.nih.gov/ij/), respectively.

Animal Preparation. All animal experiments were performed under the "Law for The Care and Welfare of Animals in Japan" and approved by the Animal Experiment Committee of Hokkaido University (approval no. 20-0118). Six-week-old BALB/c-*nu/nu* male mice were purchased from Japan SLC (Hamamatsu, Japan). The mice were allowed to acclimate to their environment for a week before cell inoculation. Cell cultures of the human-derived pancreatic ductal adenocarcinoma cell line MIA PaCa-2 (American Type Culture Collection, Manassas, Virginia) were performed as previously described.[21] Approximately 10 million MIA PaCa-2 cells were subcutaneously inoculated into the right hind legs of each BALB/c-*nu/nu* mouse. The tumor volume V was estimated using linear calipers every 2 days and calculated as $V = (\text{length} \times \text{width} \times \text{depth})\,\pi/6$. The administration of U-104 was started after the tumor volume reached 200 mm³. First, U-104 was dissolved in 55.6% polyethylene glycol 400 (PEG 400), 11.1% ethanol, and 33.3% water at 4.0 mg mL^{-1} (0.62 mmol L^{-1}) for the 20 mg per kg body weight dose or 8.0 mg mL^{-1} (1.24 mmol L^{-1}) for the 40 mg per kg body weight dose following procedures previously described for in vivo studies.[32,33] Then, this solution was administered intraperitoneally daily for 24 days at one of the two dose regimens to each of the two treatment groups. The vehicle control group received a mixture of PEG 400, ethanol, and water (100 µL in total) intraperitoneally.

In Vivo pH Mapping of the Mouse Xenograft Models. To perform pH mapping of the mouse xenograft models, dR-SG was dissolved in pure water at a concentration of 120 mmol L^{-1} and the pH was adjusted to 7.4 by adding HCl or NaOH. Mice were anesthetized by inhalation of isoflurane (initially 2.3% and then 1.0−2.0%). Each subject mouse was placed in a prone position on a mouse holder made of Rexolite 1422; the tumor-bearing leg was set at the center of the resonator in the EPR imager. Mouse body temperature and respiration rate were monitored with the fiber optic temperature sensor and small air-pressure sensor of an MR-compatible small-animal monitoring system (Model 1025, SA Instruments, Inc., Stony Brook, New York, USA). Mouse body temperature was measured from the rectum and maintained at 37 ± 0.5 °C by heated airflow regulated by the small-animal monitoring system. The tail vein was cannulated for the intravenous injection of dR-SG (7.6 mg, 0.59 mmol kg^{-1} body weight) as a bolus over 40 s. EPR spectral acquisition was started 1 min after probe injection was completed. The EPR settings for in vivo pHe mapping were the same as those for the pH mapping of the solution samples except for the incident RF power, which was set to 11.5 mW. The temperature in the central region of the tumor was invasively measured with an oxygen/temperature bare-fiber sensor (diameter 350 µm, product no. NX-BF/OT/E) of an OxyLite oxygen monitor (Oxford Optronix, Abingdon, Oxfordshire, UK). The temperatures of three xenograft tumors were measured when the volumes were between 520 and 610 mm³.

To register the EPR intensity and pHe maps to the MR anatomical maps, we first identified the base of the mouse tail in both the anatomical maps and EPR intensity maps. The 2D image matrices of the EPR intensity and pHe maps (48×48 for an FOV of 25 mm × 25 mm, pixel size 0.52 mm) were regridded to match the pixel size of the 2D MR anatomical maps (128×256 for an FOV of 40 mm × 80 mm), followed by visual alignment of the EPR intensity and pHe maps to the T_2-weighted MR anatomical maps. Tumor outlines were drawn on each T_2-weighted MR anatomical map, and the corresponding image mask was applied to the pHe maps to extract the pHe values from the entire set of 3D pHe data using ImageJ. Moreover, the tumor volume was computed by summing the product of the thickness of the slices of the MR anatomical maps and the areas of the tumor outline on each anatomical map slice to obtain a precise tumor volume of each mouse xenograft model. A spherical volume of 400 mm³ corresponds to a diameter of approximately 9 mm, so the dimensions of this tumor correspond to more than four times the spatial resolution of the image (approximately 17 pixels in our 2D pHe maps).

¹H-MR Imaging. The MR anatomical maps described above were generated from ¹H MRI scans performed immediately after EPR imaging. A ¹H mouse body coil (30 mm inner diameter; Takashima Seisakusho Co., Ltd., Tokyo, Japan) was used with a dedicated spectrometer (Japan REDOX, Ltd., Fukuoka, Japan) and a 1.5 T permanent magnet system; the same mouse holder used for the EPR measurements was also used here to maintain the mouse position. T_2-weighted, anatomical 2D images of the tumor-bearing legs were obtained using a fast spin-echo sequence and the following measurement parameters: FOV 40 mm × 80 mm, 128×256 in-plane matrix (pixel size 0.31 mm), six slices of 2 mm thickness, echo time (TE)/repetition time 16/3000
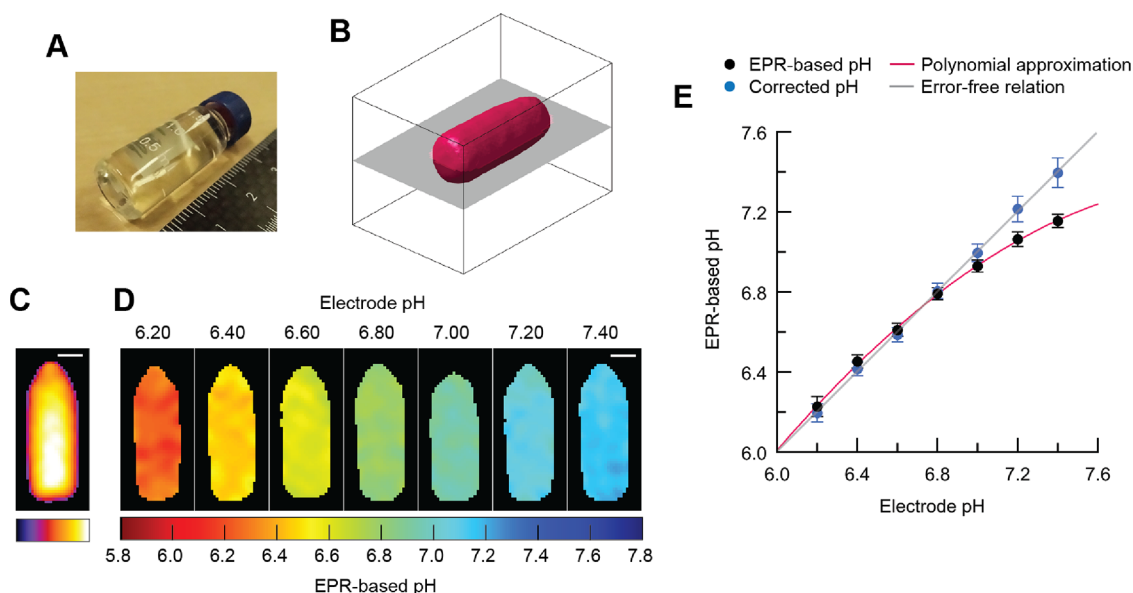
Figure 3. pH mapping of solution samples. (A) Photograph of a 2 mL vial containing dR-SG radical solution (the ruler is in centimeters). (B) The surface-rendered image of EPR signal intensities of the dR-SG vial (image matrix 48 × 48 × 72 with a field of view of 25 mm × 25 mm × 37.5 mm). (C) EPR signal intensity map at the center slice of the visualized space. (D) Reconstructed pH maps for the solution samples with different pH conditions (6.2 to 7.4 pH). (E) Linearity test between the measured and corrected pH values obtained by eq 2. Closed circles and error bars represent the mean ± standard deviation (SD) of the measured (black) and corrected (blue) pH values. The curve in red shows the cubic polynomial that best approximates the measured pH values. The scale bar represents 5 mm. In vitro pH mapping was performed at 37 °C. The concentration of dR-SG was 2 mmol L^{-1}.

ms, effective TE 64 ms, echo train 4, number of averages 4, and acquisition time 6.5 min.

RESULTS AND DISCUSSION

The MHD Receiver System Produces Twofold Sensitivity Enhancement over the Standard PSD System. To enhance the sensitivity of EPR to detect pHe in vivo, we used an MHD receiver system. The sensitivity of the modified EPR system using MHD was compared to EPR using conventional PSD to demonstrate the sensitivity enhancement of the modified EPR system.

In this study, we used the pH-sensitive nitroxyl radical probe dR-SG[30,34] in solution samples (Figure 1A). As stated in the Introduction, dR-SG is specifically designed to reflect the acidic microenvironment of the tumor and thus is a suitable molecule for assessing the sensitivity of EPR in measuring the pHe. The first-derivative EPR absorption spectrum of dR-SG has three absorption peaks (Figure 1B). The protonated and unprotonated forms of dR-SG differ in the distance between the absorption peaks in the magnetic field, called hyperfine splitting constants (HFCs); the ratio of the two forms gives the pH value of the solution.[20] Using the lineshape of the spectrum, we can estimate the proportion of two forms of dR-SG and the pH of the solution.

To demonstrate the sensitivity enhancement with MHD, we compared the SNRs of the EPR spectra measured with MHD and conventional PSD. Compared with PSD, MHD resulted in twofold sensitivity enhancement in terms of the SNR when the modulation ratio a, the ratio of the magnetic field modulation amplitude to the intrinsic peak-to-peak linewidth of the central EPR absorption peak of dR-SG, was equal to 1.

A key component of this work is the enhancement of the sensitivity of the EPR spectrometer and imager using MHD. Figure 2A shows the EPR spectra of dR-SG (2 mmol L^{-1} in phosphate-buffered saline, 2 mL of dR-SG solution) measured

with PSD and MHD. Each EPR spectrum was acquired 300 times, and the accumulated spectra are shown in Figure 2A. In MHD, we apply the amplitude of magnetic field modulation, which is not small compared to the intrinsic linewidth of the spectrum, to the electron spin system. This modulation reveals the non-linear response of the acquired signal in the time domain. Such a signal has multiple harmonic components in the Fourier domain. A difference in the amplitude of magnetic field modulation influences the generation of higher-order harmonics. The spectrum recorded with MHD was reconstructed with the first to fourth harmonics at a modulation ratio, that is, the ratio of the magnetic field modulation amplitude to the intrinsic peak-to-peak linewidth of the central EPR absorption peak, of $a = 1.0$. The first to fifth harmonics acquired at a modulation ratio of $a = 2.0$ are depicted in Figure 2B. The detected harmonics were accumulated 300 times and denoised during signal processing using low-pass filtering. For spectral reconstruction, the cutoff frequency of the LPF was set to the 50th index of the data array in the Fourier domain at $a = 1.0$ and the 52nd index of the data array at $a = 2.0$ to suppress high-frequency noise. This filtering was optimized for recovering the linewidth of the EPR spectra at a given modulation ratio. Figure 2C,D shows the SNR and the peak-to-peak linewidth of the EPR spectra, respectively, as a function of the number of harmonics involved. Figure 2E shows the SNR variance of the 300 EPR spectra obtained from the same solution sample with PSD and MHD. The mean of the SNR was 8 at $a = 0.25$ and 21 at $a = 1.0$ with PSD. In contrast, the mean SNR was 41 at $a = 1.0$ and 40 at $a = 2.0$ with MHD. We achieved twofold sensitivity enhancement of the EPR spectrometer setup, which is beneficial for pHe mapping in mouse xenograft models. If we apply low-pass filtering to the standard first-derivative spectrum to further improve the SNR, the SNR may be improved but at the cost of
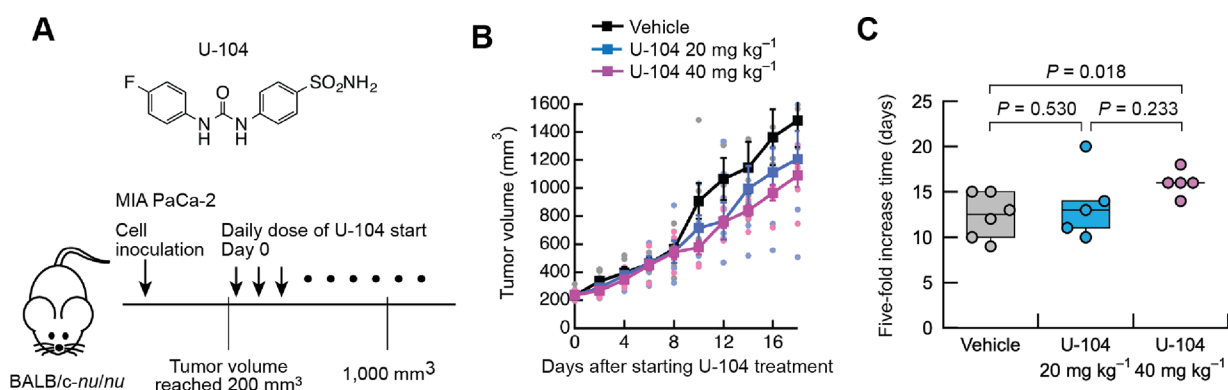
Figure 4. Tumor growth delay due to U-104 treatment. (A) Chemical structure of the CAIX inhibitor U-104 and its administration plan for this experiment. Approximately 10 million MIA PaCa-2 cells were subcutaneously inoculated into the right hind legs of each mouse. (B) Tumor growth curves for the three dose groups. Closed squares and error bars represent the mean ± standard error (SE). Individual tumor volumes are represented as closed circles colored to match the lines. (C) Time at which a fivefold increase in tumor volume (200 to 1000 mm^3) occurred. Individual times are shown in matched color-filled circles for each group. The sample sizes during the tumor growth monitoring experiment were 6 for the vehicle control group, 5 for the group treated with 20 mg per kg body weight U-104, and 5 for the group treated with 40 mg per kg body weight U-104.

lineshape distortion due to a slow response of low-pass filtering.

pH Mapping Using MHD Shows Reasonable Accuracy and Resolution in the Physiological pH Range. We mapped the solution samples with known pH values to ensure the accuracy and resolution of pH mapping with MHD. The accuracy and resolution of pH mapping are essential for sensitively measuring the pH of solution samples and that of the TME in animal models in vivo. Therefore, we investigated whether our pH mapping system has reasonable accuracy and resolution for solution samples with known pH values. Given its high accuracy, an electrode-based pH meter was used to measure the pH of the solution samples and the obtained values were used as the reference values against EPR-based pH mapping.

Using dR-SG (2 mmol L^{-1} in phosphate-buffered saline) and the 750 MHz EPR spectrometer described above, we performed 3D pH mapping of the solution samples contained in 2 mL vials (Figure 3A). The pKa of the dR-SG radical is 6.60 at 37 °C and 6.84 at 23 °C.[34] Since the pKa of the dR-SG radical is temperature-dependent, the temperature at the measurement position should be taken into account in pH mapping. However, the physiological range of temperature in a mouse's tumor tissue does not compromise the EPR-based pH measurement because the effect of a pKa shift against a few degrees Celsius (for example, 6.60 at 37 °C vs 6.63 at 35 °C) is well below the measurement resolution of pH mapping. As we maintained the temperature of the samples to 37 °C, we set the pKa to 6.60 pH for pH mapping. We used the ART with 3375 spectral projections[21,31] to reconstruct the surface-rendered images of the EPR signal intensity for dR-SG (Figure 3B). The slice-selective signal intensity map at the center of the 3D visualized space showed that the detectable region of our EPR imaging sufficiently covered the radical solution in the vial (Figure 3C). We then mapped the pH of dR-SG solutions with pH values of 6.2–7.4 and found that our pH mapping can respond to the different pH values of dR-SG solutions and offered reasonable spatial uniformity of pH detection (Figure 3D). Moreover, calculation of the quantitative relation between the pH values obtained with EPR and the reference pH values using the least squares method (Figure 3E) showed that the curve that best fit the EPR-based pH values (pH$_{EPR}$)

and the electrode pH values can be expressed by a cubic polynomial. Following eq 1, we computed the corrected pH value for the EPR (pH$_{corrected}$) to improve the linearity of the measurements. Lin's concordance correlation coefficients for the EPR-based and corrected pH values (pH$_{EPR}$ and pH$_{corrected}$ in eq 2) and standard electrode pH values are 0.9519 and 0.9997, respectively, in Figure 3E. This means that our correction of pH values improves the agreement between the EPR and standard electrode measurements.

When the absolute difference between the pH of the solution and the pKa of dR-SG is large, the shift in the ratio of the two dR-SG forms is small, leading to the error observed in the high pH region. However, the error between the pH value measured with the electrode pH meter and the mean pH value from EPR-based mapping ranged from +0.056 to −0.027 pH units over the 6.2–7.4 corrected pH range (Figure 3E and Supplementary Table 2), suggesting that the errors of the EPR-based pH values from the reference pH values are quite small compared to the resolution of the pH measurements (see the discussion of the pH resolution below). The dR-SG radical loses sensitivity for pH when the pH value is far from the pKa. Moreover, since the pKa of the dR-SG radical is dependent on the temperature, the correction of EPR-based pH values using an empirically obtained cubic polynomial in eq 2 can depend on the temperature. Therefore, the polynomial for correcting the measured pH values (pH$_{EPR}$, eq 1) should fit the given temperature condition and pH range as well as the measurement settings.

In addition, it was essential to ensure that EPR-based pH maps obtained with MHD had lower or similar systemic errors to those obtained with the conventional PSD system. We assessed the systematic error in EPR-based pH mapping using the difference from the corresponding electrode-based pH value and found it to be similar to that obtained with PSD (Supplementary Table 2).

We next quantified the resolution of the pH measurements. By modeling the measurements as Gaussian distribution, we quantified the resolution as the full width at half-maximum [2 (2 log$_e$ 2)$^{1/2}$ SD = 2.35 SD]. At a pKa of 6.60 (37 °C), the pH measurement resolution was 0.094 (SD = 0.040; see Supplementary Table 2) after correction using eq 2 for the data shown in Figure 3E. Moreover, the corrected pH
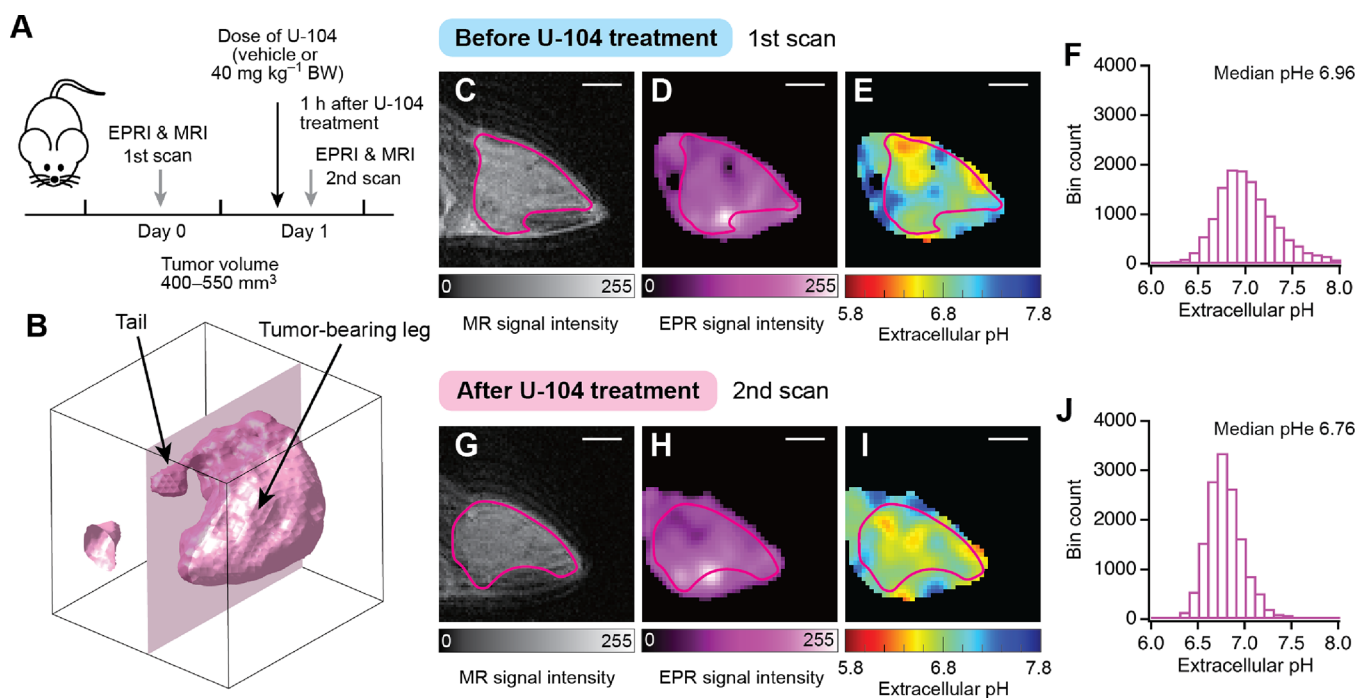
Figure 5. Influence of U-104 treatment on extracellular pH (pHe) in MIA PaCa-2 mouse xenograft models. (A) Experimental plan for extracellular pH (pHe) mapping and single U-104 administration. (B) Surface-rendered image of the EPR signal intensities for a representative tumor-bearing leg (image matrix 48 × 48 × 48 with FOV of 25 mm × 25 mm × 25 mm), (C, G) MR anatomical maps, (D, H) EPR signal intensity maps, (E, I) pHe maps, and (F, J) histograms of tumor pHe before and after U-104 treatment, respectively. The 2D EPR and pHe maps have an image matrix of 48 × 48 with an FOV of 25 mm × 25 mm. The scale bar represents 5 mm. At the time of both scans, the mice weighed 20 to 26 g. The pHe maps in (E) and (I) were obtained with 20% maximum intensity thresholding in the corresponding EPR signal intensity maps.

resolution was 0.096 at a pH of 7.0 (SD = 0.041). A complete list of the pH measurement resolution and error for each sample is given in Supplementary Table 2. As shown here, we achieved reasonable accuracy and resolution of pH mapping with MHD for the known-pH solutions that differed in pH by 0.2 pH units.

Treatment with 40 mg per kg Body Weight of the CAIX Inhibitor U-104 Results in Tumor Growth Delay in Mouse Xenograft Models. After proving the sensitivity, accuracy, and resolution of our EPR-based pH mapping system using pH solutions in vitro, we explored whether it can be used to detect changes in pHe in vivo following treatment with the CAIX inhibitor U-104.

To ensure that U-104 treatment led to changes in pHe, we first needed to determine the dose of U-104 that delays tumor growth in the mouse xenograft model. To this end, we longitudinally monitored the growth of MIA PaCa-2 tumors implanted in mice that received daily intraperitoneal injections of 20 or 40 mg per kg body weight of U-104 or vehicle (control group) after the tumor volume reached 200 mm³ (Figure 4A). The doses of U-104 used were based on those used in a previous study of mouse xenograft models.[31] Differences in the tumor volume between the three groups were evident 10 days after the start of U-104 administration (Figure 4B). However, when the tumor growth speeds (calculated as the number of days required for the tumors to increase their volumes five folds [200 to 1000 mm³]) were compared, only the difference between the group treated with 40 mg per kg body weight of U-104 (n = 5) and the vehicle control group (n = 6) was statistically significant (P = 0.018, two-sided Student's t test) (Figure 4C). Given these findings and the fact that the 40 mg per kg body weight U-104-treated

group did not show any side effects, we chose this dose for the subsequent experiments.

U-104 Treatment Shows a Tendency toward Further Extracellular Acidification in Tumors. Metabolic shifts resulting from U-104 treatment may initiate a change in the pHe in the microenvironment of xenograft tumors. To clarify this response, the pHe of the xenograft tumors was monitored before and after U-104 treatment, which affects tumor pH homeostasis, in both the U-104-treated group and the vehicle control group.

To demonstrate in vivo pHe mapping, we monitored the pHe of MIA PaCa-2 tumors that had reached the volume of 400−550 mm³ before (day 0) and 1 h after the intraperitoneal injection of 40 mg per kg body weight of U-104 (day 1) (Figure 5A). We chose this tumor volume for pHe mapping, because low SNRs of the EPR signals from dR-SG limited in vivo pHe mapping for small tumors below 400 mm³. At both time points, the scans for constructing the 3D maps (Figure 5B,D,H) were performed with EPR followed by multislice anatomical maps with T_2-weighted ^{1}H-MRI (Figure 5C,G). The mean temperature of the three xenograft tumors was 35 °C (n = 3); therefore, we set the pKa to perform the pHe mapping to 6.63. These three mice are different than those in the U-104-treated and vehicle control groups.

The use of MHD to enhance the sensitivity of EPR imaging facilitated our pHe mapping of xenograft tumors in vivo by enabling the measurement of smaller tumors, which in our study were approximately half the size of those previously measured by EPR-based pH mapping.[21] A higher EPR signal sensitivity is required for the pHe mapping of smaller xenograft tumors for MIA-PaCa-2 cells. To obtain a stronger EPR signal intensity from the tumor, it is necessary to increase the uptake

of the dR-SG radical into the tumor. Uptake of the dR-SG radical depends on angiogenesis, outgrowth of malignant tissue beyond the vasculature, and necrosis-like cores within tumors. These factors influence the state of tumor perfusion and, finally, the EPR signal intensity. In addition, we were able to reduce the concentration of dR-SG required for intravenous injection, i.e., 120 versus 150 mmol L^{-1} in a previous report.[21] A reduction in the probe concentration is vital for small-animal studies in practice because dR-SG is precious and requires multi-step organic synthesis (15 steps).[30] We determined this probe concentration to obtain the reasonable SNR for pHe mapping in vivo. Moreover, a technical concern in pHe mapping using the dR-SG probe is the possibility of pH alteration due to the probe being a buffer. In an MR spectroscopic imaging study on tumor pH in a mouse model of prostate cancer by Ibrahim et al., they pointed out a caution in the pH measurements, i.e., higher steady-state concentrations of an MR spectroscopy imaging agent (a non-volatile buffer, 2-imidazole-1-yl-3-ethoxycarbonylpropionic acid (IEPA), with a pKa of 6.9) can be associated with "the risk that IEPA itself may alter the pH that is sought to be measured".[35] To reduce the risk of pH alteration due to the dR-SG radical itself, lower concentrations of the dR-SG radical are preferable and require an EPR spectrometer with a greater detection sensitivity for mouse tumor model experiments. Furthermore, the median pHe for all MIA PaCa-2 xenograft tumors was estimated to be 7.004 ± 0.027 pH (mean $\pm$ SE, $n = 11$) before U-104 treatment, consistent with the values obtained for the same xenograft models in our previous study (7.05 pH).[21] This consistency in pHe detection suggests that EPR-based pH mapping can be highly reproducible.

Using EPR, we obtained the 3D pHe maps of the tumors (Figure 5E,I) and observed a shift in the pHe after U-104 treatment (Figure 5F,J). Furthermore, the pHe histogram before U-104 treatment was more broadly distributed than that obtained after U-104 treatment. This is because the correction of the pH with the third-order polynomial (eq 2) may enhance the error of pHe in a high-pHe region such as that included in the pHe map obtained before U-104 treatment. Since the pHe values close to the pKa of dR-SG can be measured more precisely, the pHe maps after U-104 treatment, which are more acidic than the pHe maps before U-104 treatment, have minor variance. Statistical tests of the pHe shift, the tumor volume, and the acidic volume fraction of the tumors with U-104 treatment are given in the Supporting Information (Figure S1). To further gain the data on extracellular acidification, the tumor cell response to U-104 treatment in vitro is also given in the Supporting Information (Supplementary Methods and Note, Figures S2, S3, and S4). These data for extracellular pH and energy metabolism assays in vitro suggest that EPR-based pHe mapping using MHD accurately reflects the pHe shift after U-104 treatment in vivo. Moreover, MCT4 expression and hypoxic area in tumor tissues before and after U-104 treatment were observed to pursue a real condition in xenograft tumors (Supporting Information Figure S5). We found that the results of our pHe mapping reflected the pHe shifts due to U-104 treatment, instead of any change in MCT4 expression.

When U-104 inhibits CAIX, i.e., the conversion of carbon dioxide to bicarbonate and H^+, the amount of H^+ in the extracellular medium should be reduced, suggesting a higher pHe. However, U-104 also affects the metabolism of MIA PaCa-2 cells, such as the oxygen consumption rate (Supporting

Information Figure S3). The previous study by Lee et al. suggested that U-104 increased lactate production without significantly changing glucose consumption and induced extracellular acidosis.[36] Due to the overall effects of U-104 treatment, U-104 treatment leads to a tendency toward further extracellular acidification in tumors. Further investigation of cellular metabolism and U-104 treatment should be performed to clarify the mechanism of the trend in extracellular acidification and the metabolic shift in cancer cells due to U-104.

There are three distinctive characteristics of EPR-based pH mapping compared to MRI, i.e., (i) higher sensitivity of exogenous probes, (ii) acquisition time, and (iii) a variety of pH-sensitive radical probes. One of the differences between NMR- and EPR-based techniques in pH mapping is the sensitivity of exogenous imaging probes. As we mentioned in the Introduction, the electron gyromagnetic ratio is 658 times higher than the ratio of a proton. This advantage of EPR detection makes a difference in the concentrations of exogenously infused imaging probes in EPR and CEST-MRI. In the multislice CEST-MRI described by Randtke et al., they used a 200 μL bolus injection of iopamidol at 788 mmol L^{-1}, followed by a 200 μL h^{-1} infusion of iopamidol.[18] In contrast, 3D EPR-based pHe mapping used a 100 μL bolus injection of dR-SG at 120 mmol L^{-1}. Furthermore, 30 mmol L^{-1} iopamidol solution was used in multislice CEST-MRI[19] and 2 mmol L^{-1} dR-SG solution was used in EPR-based 3D pH mapping for the phantom experiments.

Moreover, the acquisition times of 3D pHe mapping and multislice CEST MRI are different. In the present work, EPR-based 3D pHe mapping requires 7.5 min for image acquisition. In contrast, the eight slices with multislice CEST-MRI described by Villano et al. require less than 10 min.[19] While these acquisition times are not significantly different, EPR-based 3D pHe mapping has room for further reductions in acquisition time without changing the acquisition protocol by reducing the magnetic field scan duration by one order of magnitude.[37]

An imaging agent approved by a national regulatory agency is essential for clinical applications of pH mapping with CEST-MRI. Therefore, iopamidol is extensively used even in preclinical studies. In contrast, EPR can use a variety of pH-sensitive radicals in addition to the dR-SG radical. For example, the p_1-TAM radical has multi-functional sensitivities to pH, the partial pressure of oxygen, and inorganic phosphate [Pi].[38] The selection of exogenous radical probes can provide different information with EPR, such as multi-functional mapping, without changing the acquisition protocol. EPR-based pHe mapping can currently show these features only in preclinical settings and is an emerging mapping method for mouse tumor models.

■ CONCLUSIONS

Our results showed the feasibility of in vivo tumor pHe mapping using EPR to monitor pharmacological intervention in tumor xenograft models. In particular, the sensitivity enhancement of the modified EPR system using MHD was beneficial to apply pHe mapping to mouse xenograft models in vivo. The previous study of pHe mapping using EPR showed extracellular acidification in mouse xenograft models; however, the tumor response to pharmacological intervention was not investigated. This ability to visualize the tumor pHe can be useful to investigate the response of the TME to any anticancer

drug. As a proof of concept, we applied the developed EPR system to monitor pHe treatment with the CAIX inhibitor U-104, which allowed us to detect a shift in tumor median pHe. While we showed only the effects of U-104 on tumor xenografts of the MIA PaCa-2 cell line, different tumor xenograft models and metabolic pathway-targeting inhibitors should be investigated using in vivo pHe mapping to better understand the tumor response to pharmacological intervention and, in general, the TME of solid tumors. In this way, the tumor pHe mapping method can serve as a practical approach to the early assessment of the tumor response to cancer treatment in preclinical studies. Furthermore, monitoring pHe can also be used for the development of improved metabolism-targeting cancer treatments.

ASSOCIATED CONTENT

Ⓢ Supporting Information

The Supporting Information is available free of charge at https://pubs.acs.org/doi/10.1021/acs.analchem.2c03194.

> Additional methods, data, and notes for the results, including statistical tests for the influence of U-104 treatment on the tumors, titration curve of the R-SG radical, tumor cell response to U-104 treatment, cell viability, and immunostained tissue section (PDF)

AUTHOR INFORMATION

Corresponding Author

Hiroshi Hirata — *Division of Bioengineering and Bioinformatics, Faculty of Information Science and Technology, Hokkaido University, Sapporo 060-0814, Japan;* ⓘ orcid.org/0000-0002-6906-1608; Email: hhirata@ist.hokudai.ac.jp

Authors

Ririko Nakaoka — *Division of Bioengineering and Bioinformatics, Graduate School of Information Science and Technology, Hokkaido University, Sapporo 060-0814, Japan*

Kazuhiro Kato — *Laboratory of Radiation Biology, Graduate School of Veterinary Medicine, Hokkaido University, Sapporo 060-0818, Japan*

Kumiko Yamamoto — *Laboratory of Radiation Biology, Graduate School of Veterinary Medicine, Hokkaido University, Sapporo 060-0818, Japan;* Present Address: Department of Food, Aroma and Cosmetic Chemistry, Faculty of Bioindustry, Tokyo University of Agriculture, Abashiri-shi, Hokkaido 099-2493, Japan; ⓘ orcid.org/0000-0002-5669-8204

Hironobu Yasui — *Laboratory of Radiation Biology, Faculty of Veterinary Medicine, Hokkaido University, Sapporo 060-0818, Japan*

Shingo Matsumoto — *Division of Bioengineering and Bioinformatics, Faculty of Information Science and Technology, Hokkaido University, Sapporo 060-0814, Japan*

Igor A. Kirilyuk — *N.N. Vorozhtsov Novosibirsk Institute of Organic Chemistry, Novosibirsk 630090, Russia;* ⓘ orcid.org/0000-0001-6033-0368

Valery V. Khramtsov — *Department of Biochemistry and Molecular Medicine, and In Vivo Multifunctional Magnetic Resonance Center, West Virginia University Robert C. Byrd Health Sciences Center, Morgantown, West Virginia 26506, United States;* ⓘ orcid.org/0000-0001-6187-5546

Osamu Inanami — *Laboratory of Radiation Biology, Faculty of Veterinary Medicine, Hokkaido University, Sapporo 060-0818, Japan*

Complete contact information is available at:
https://pubs.acs.org/10.1021/acs.analchem.2c03194

Notes

The authors declare no competing financial interest.

ACKNOWLEDGMENTS

REFERENCES

(1) Michiels, C.; Tellier, C.; Feron, O. *Biochim. Biophys. Acta* **2016**, *1866*, 76−86.

(2) Wojtkowiak, J. W.; Verduzco, D.; Schramm, K. J.; Gillies, R. J. *Mol. Pharmaceutics* **2011**, *8*, 2032−2038.

(3) Corbet, C.; Feron, O. *Nat. Rev. Cancer* **2017**, *17*, 577−593.

(4) Peppicelli, S.; Bianchini, F.; Calorini, L. *Cancer Metastasis Rev.* **2014**, *33*, 823−832.

(5) Swietach, P.; Vaughan-Jones, R. D.; Harris, A. L. *Cancer Metastasis Rev.* **2007**, *26*, 299−310.

(6) Ganapathy-Kanniappan, S.; Geschwind, J.-F. H. *Mol. Cancer* **2013**, *12*, 152.

(7) Macheda, M. L.; Rogers, S.; Best, J. D. *J. Cell. Physiol.* **2005**, *202*, 654−662.

(8) Denko, N. C. *Nat. Rev. Cancer* **2008**, *8*, 705−713.

(9) Supuran, C. T. *Nat. Rev. Drug. Discovery* **2008**, *7*, 168−181.

(10) Lee, S.-H.; McIntyre, D.; Honess, D.; Hulikova, A.; Pacheco-Torres, J.; Cerdán, S.; Swietach, P.; Harris, A. L.; Griffiths, J. R. *Br. J. Cancer* **2018**, *119*, 622−630.

(11) Chen, Y. *Anal. Biochem.* **2021**, *612*, 113900.

(12) Takahashi, S.; Kagami, Y.; Hanaoka, K.; Terai, T.; Komatsu, T.; Ueno, T.; Uchiyama, M.; Koyama-Honda, I.; Mizushima, N.; Taguchi, T.; Arai, H.; Nagano, T.; Urano, Y. *J. Am. Chem. Soc.* **2018**, *140*, 5925−5933.

(13) Gallagher, F. A.; Kettunen, M. I.; Day, S. E.; Hu, D.-E.; Ardenkjær-Larsen, J. H.; Zandt, R. I.; Jensen, P. R.; Karlsson, M.; Golman, K.; Lerche, M. H.; Brindle, K. M. *Nature* **2008**, *453*, 940−943.

(14) Düwel, S.; Hundshammer, C.; Gersch, M.; Feuerecker, B.; Steiger, K.; Buck, A.; Walch, A.; Haase, A.; Glaser, S. J.; Schwaiger, M.; Schilling, F. *Nat. Commun.* **2017**, *8*, 15126.

(15) Longo, D. L.; Bartoli, A.; Consolino, L.; Bardini, P.; Arena, F.; Schwaiger, M.; Aime, S. *Cancer Res.* **2016**, *76*, 6463−6470.

(16) High, R. A.; Randtke, E. A.; Jones, K. M.; Lindeman, L. R.; Ma, J. C.; Zhang, S.; LeRoux, L. G.; Pagel, M. D. *Neoplasia* **2019**, *21*, 1085−1090.

(17) Buyse, C.; Joudiou, N.; Corbet, C.; Feron, O.; Mignion, L.; Flament, J.; Gallez, B. *Cancers* **2021**, *13*, 4278.

(18) Randtke, E. A.; Granados, J. C.; Howison, C. M.; Pagel, M. D.; Cárdenas-Rodríguez, J. *Magn. Reson. Med.* **2017**, *78*, 97−106.

(19) Villano, D.; Romdhane, F.; Irrera, P.; Consolino, L.; Anemone, A.; Zaiss, M.; Dastrù, W.; Longo, D. L. *Magn. Reson. Med.* **2021**, *85*, 1335−1349.

(20) Schweiger, A.; Jeschke, G. *Principles of pulsed electron paramagnetic resonance*; Oxford University Press: New York, 2001; pp. 518−521.

(21) Komarov, D. A.; Ichikawa, Y.; Yamamoto, K.; Stewart, N. J.; Matsumoto, S.; Yasui, H.; Kirilyuk, I. A.; Khramtsov, V. V.; Inanami, O.; Hirata, H. *Anal. Chem.* **2018**, *90*, 13938−13945.

(22) Hyodo, F.; Matsumoto, K.-I.; Matsumoto, A.; Mitchell, J. B.; Krishna, M. C. *Cancer Res.* **2006**, *66*, 9921−9928.

(23) Bikineev, V. A.; Zavatskii, E. A.; Isaev-Ivanov, V. V.; Lavrov, V. V.; Lomakin, A. V.; Fomichev, V. N.; Shabalin, K. A. *Tech. Phys.* **1995**, *40*, 619−625.

(24) Tseitlin, M.; Eaton, S. S.; Eaton, G. R. *J. Magn. Reson.* **2011**, *209*, 277−281.

(25) Yu, Z.; Tseytlin, M.; Eaton, S. S.; Eaton, G. R. *J. Magn. Reson.* **2015**, *254*, 86−92.

(26) Gonet, M.; Baranowski, M.; Czechowski, T.; Kucinska, M.; Plewinski, A.; Szczepanik, P.; Jurga, S.; Murias, M. *Free Radical Biol. Med.* **2020**, *152*, 271−279.

(27) Sato-Akaba, H.; Fujii, H.; Hirata, H. *Rev. Sci. Instrum.* **2008**, *79*, 123701.

(28) Sato-Akaba, H.; Kuwahara, Y.; Fujii, H.; Hirata, H. *Anal. Chem.* **2009**, *81*, 7501−7506.

(29) Kawada, Y.; Hirata, H.; Fujii, H. *J. Magn. Reson.* **2007**, *184*, 29−38.

(30) Samouilov, A.; Efimova, O. V.; Bobko, A. A.; Sun, Z.; Petryakov, S.; Eubank, T. D.; Trofimov, D. G.; Kirilyuk, I. A.; Grigor'ev, I. A.; Takahashi, W.; Zweier, J. L.; Khramtsov, V. V. *Anal. Chem.* **2014**, *86*, 1045−1052.

(31) Komarov, D. A.; Hirata, H. *J. Magn. Reson.* **2017**, *281*, 45−50.

(32) Lock, F. E.; McDonald, P. C.; Lou, Y.; Serrano, I.; Chafe, S. C.; Ostlund, C.; Aparicio, S.; Winum, J.-Y.; Supuran, C. T.; Dedhar, S. *Oncogene* **2013**, *32*, 5210−5219.

(33) Ramchandani, D.; Unruh, D.; Lewis, C. S.; Bogdanov, V. Y.; Weber, G. F. *Lab. Invest.* **2016**, *96*, 1234−1245.

(34) Bobko, A. A.; Eubank, T. D.; Voorhees, J. L.; Efimova, O. V.; Kirilyuk, I. A.; Petryakov, S.; Trofimiov, D. G.; Marsh, C. B.; Zweier, J. L.; Grigor'ev, I. A.; Samouilov, A.; Khramtsov, V. V. *Magn. Reson. Med.* **2012**, *67*, 1827−1836.

(35) Ibrahim Hashim, A.; Cornnell, H. H.; Coelho Ribeiro, M. d. L.; Abrahams, D.; Cunningham, J.; Lloyd, M.; Martinez, G. V.; Gatenby, R. A.; Gillies, R. J. *Clin. Exp. Metastasis* **2011**, *28*, 841−849.

(36) Lee, J. Y.; Onanyan, M.; Garrison, I.; White, R.; Crook, M.; Alexeyev, M. F.; Kozhukhar, N.; Pastukh, V.; Swenson, E. R.; Supuran, C. T.; Stevens, T. *Am. J. Physiol.: Lung Cell. Mol. Physiol.* **2019**, *317*, L188−L201.

(37) Komarov, D. A.; Samouilov, A.; Hirata, H.; Zweier, J. L. *J. Magn. Reson.* **2021**, *329*, 107024.

(38) Taguchi, A.; DeVience, S.; Driesschaert, B.; Khramtsov, V. V.; Hirata, H. *Analyst* **2020**, *145*, 3236−3244.